Research Paper

Three-Dimensional Freehand Ultrasound Strain Elastography Based on the Assessment of Endogenous Motion: Phantom Study

Andrius SAKALAUSKAS[(1)], Rytis JURKONIS[(2)*], Arūnas LUKOŠEVIČIUS[(2)]

[(1)] *TELEMED, Ultrasound Medical Systems*
Vilnius, Lithuania

[(2)] *Biomedical Engineering Institute, Kaunas University of Technology*
Kaunas, Lithuania

*Corresponding Author e-mail: rytis.jurkonis@ktu.lt

The purpose of this paper is to present the results of the pilot experiments demonstrating proof of concept of three-dimensional strain elastography, based on freehand ultrasound for the assessment of strain induced by endogenous motion. The technique was tested by inducing pulsatility in an agar-based tissue mimicking phantom with inclusions having different stiffness and scanning the 1D array with an electromagnetic position sensor. The proof of concept is explored with a defined physical phantom and the adopted algorithm for strain analysis. The agar-based phantom was manufactured with two cylindrical inclusions having different stiffness (7 kPa and 75 kPa in comparison to the background 25 kPa) and scattering properties. The internal strain in the phantom was introduced by mimicking a pulsating artery. The agar mixture displacements were estimated by using the GLUE algorithm. The 3D isosurfaces of inclusion from rendered volumes obtained from the B-mode image set and strain elastograms were reconstructed and superimposed for a quantitative comparison. The correspondence between the B-mode image-based inclusion volume and the strain elastography-based volume was good (the Jaccard similarity coefficient in the range 0.64–0.74). The obtained results confirm the 3D freehand endogenous motion-based elastography as a feasible technique. The visualization of the inclusions was successful. However, quantitative measurements showed that the accuracy of the method in volumetric measurements is limited.

Keywords: strain elastography; endogenous motion; freehand scanning; 3D imaging; tissue mimicking phantom.
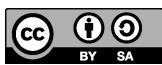
1. Introduction

Strain elastography is one of the techniques used for the assessment of tissue stiffness and has been shown to be efficient in the diagnostics of breast lesions (DIETRICH *et al.*, 2017), thyroid (COSGROVE *et al.*, 2017), prostate (BARR *et al.*, 2017), and other areas. The strain elastography measures slight tissue deformations (strain range 0.1–2%), which are typically induced by external compression by an ultrasound probe (WELLS, LIANG, 2011). The algorithm calculates the axial displacements between the consecutive RF data frames and the strain estimates are obtained by taking the spatial derivative in the axial direction (DIETRICH *et al.*, 2017). The obtained strain values are color coded and the two-dimensional (2D) strain image is superimposed on the structural B-mode image, which is based on the reflection magnitude. The scanning specialist interprets both images and measures parameters of the region of interest (ROI), such as the strain ratio or the elasticity score. Overall, the strain elastography is a qualitative technique due to unknown stress, but still provides the relative information about tissue stiffness (DIETRICH *et al.*, 2017). Unfortunately, the strains induced by the probe can be estimated only in the case of tissue, which are relatively superficial (up to few centimeters), and the deeper structures cannot be observed and assessed by the technique, be-

cause uniform strain cannot be induced in deeper layers. Fortunately, there are other ways to implement strain elastography by employing endogenous motion and strain of tissue, which are caused due to the natural pulsatility of blood vessels and the beating heart. The strain elastography based on endogenous motion was pioneered by the authors (DICKINSON, HILL, 1982; WILSON, ROBINSON, 1982; TRISTAM *et al.*, 1986). Endogenously induced strain could also be employed for imaging purposes. The phantom study with internal deformation caused by pressure variation in the vessel is presented in (MAI, INSANA, 2002). The initial experiments of endogenous strain assessment and imaging were performed by our group (ZAMBACEVIČIENĖ *et al.*, 2019; SAKALAUSKAS *et al.*, 2018). Later, it was found that the parameters derived from the two-dimensional images of endogenous strain have a correlation with different stages of liver fibrosis (SAKALAUSKAS *et al.*, 2019) and portal hypertension (GELMAN *et al.*, 2020).

Three-dimensional (3D) elasticity imaging in clinical practice is still limited, manufacturers of ultrasound scanners and the scientific community are still improving this modality. Three-dimensional imaging by using matrix arrays is limited by the frame rate and spatial resolution, which are typically lower for 2D arrays (LEE *et al.*, 2018). The 2D matrix array technology requires very sophisticated electronics to deal with very large number of channels connected to array elements. Fortunately, it is possible to implement 3D volume acquisition by using a conventional one-dimensional (1D) array probe and a mechanical linear scanner (HUANG *et al.*, 2015; HENDRIKS *et al.*, 2016; RICHARDS *et al.*, 2009), or a 3D transducer translating mechanical device (CHEN *et al.*, 2016). A much cheaper and relatively simple method could be implemented only by attaching a position tracking sensor to an ultrasound probe (GILJA *et al.*, 1998, WANG *et al.*, 2013). This enables so-called freehand 3D mode (MOZAFFARI, LEE, 2017). The comparison of simulated 3D strain imaging with the mechanically swept probe and freehand scanning (HOUSDEN *et al.*, 2010) has shown that it is possible to produce a good strain images using the freehand method, which may be preferable in clinical practice. The freehand 3D ultrasound imaging in the B-mode was extensively reviewed by MOZAFFARI and LEE (2017). The most of reviewed B-mode systems employed optical or electromagnetic position tracking solutions. But only several approaches to implement elastography by using 1D array probe and position sensor could be found (LEE *et al.*, 2018; LINDOP *et al.*, 2006). LINDOP *et al.* (2006) used an optical position tracking system for 3D quasistatic elastography, meanwhile LEE *et al.* (2018) proposed to use an electromagnetic one. Both groups successfully conducted 3D freehand strain elastography experiments and demonstrated the feasibility of the method. However, these methods applied external pressure by the operator to induce strain by the scanning probe. This makes the scanning procedure quite complicated since the probe movements should meet the simultaneous requirements of strain induction and scanning of volume. An external strain induction source based on the use of applied low frequency vibrator was demonstrated on the phantom (BERCOFF *et al.*, 2004). A similar motorized 3D vibro-elastography method also uses induced harmonic motion and synchronous strain measurements (ABEYSEKERA *et al.*, 2015), but both methods are not adapted to clinically preferable freehand scanning.

Fortunately, external deformation or vibration potentially could be substituted by endogenous excitation induced by natural cardiovascular activity. Initial publications on the endogenous cardiovascular motion application showed its potential for liver elasticity imaging (KOLEN *et al.*, 2004), also for thyroid nodule diagnostics using carotid artery pulsation (BAE *et al.*, 2006) and diastolic strain variation (LUO *et al.*, 2009). This approach could have advantage, since 3D scanning using 1D array will not require to apply the uniform compression at the same time, that might be not so easy to accomplish by scanning by the performing operator. In case of endogenous motion, the probe can be moved completely freehand without the requirement to make uniform pushes to induce strain. However, the displacements and, respectively, a strain magnitude for the endogenous excitation are frequently much lower and omnidirectional comparing with the ones induced externally but it is not so easy to measure them. This leads to high requirements for the specificity of the displacement estimation algorithm, especially in the case of 3D imaging of a dynamic structure.

The purpose of this paper is to present the proof of concept of 3D strain elastography, based on strain induced by endogenous motion and freehand 3D ultrasound imaging. To the best of our knowledge there are no published scientific papers, which deal with endogenous motion-based 3D elastography and we see our novelty in the phantom-based analysis of strain endogenous excitation and its application for 3D fused strain and B-mode imaging. The method was tested by inducing pulsatility in the agar-based tissue mimicking phantom with cylindrical inclusions having different stiffness and scattering properties in comparison to the background material. The strain-based volumes of the inclusions were evaluated and compared to volumes obtained from B-mode images for a quantitative assessment.

2. Materials and methods

2.1. Scanner and preset

The ultrasound scanner Ultrasonix Sonix Touch (Analogic Corporation, Peabody, MA, USA), which allows the collection of raw RF signals from all scanning

lines, equipped with the linear array transducer (L14–5/38 GPS, 128 acoustic elements) was used for data collection in this study.

The main parameters of ultrasonic scanning were as follows: scanning depth – 7 cm, ultrasound frequency – 13.3 MHz, transmit single focal depth – 3.5 cm. RF data were recorded in 314 scanning lines per the B-scan frame, the frame rate – 27 Hz. The RF signal digitized with 40 MHz sampling frequency and the analog-to-digital converter resolution 16 bits.

The ultrasound scanner has the ability to measure the position and orientations of the linear probe by the electromagnetic tracking system trakSTAR (Ascension, Yarraville, Australia) incorporated with the ultrasound scanner by a manufacturer. According to the specification from a manufacturer the accuracy of a static position is 1.4 mm RMS and 0.5° RMS of a static orientation angle. Sequences of B-scan images the RF signals and 3D position data were acquired and stored for later offline processing.

2.2. Phantom

An experimental phantom, mimicking tumor foci in the liver, was produced. The liver-mimicking phantom having two inclusions with different stiffness was made from agar mixtures. The surrogate endogenous motion was induced by mimicking a pulsating artery. The background of the phantom was manufactured by mixing 10 g/l agar concentration in distilled water. The agar powder was slowly stirred until it was fully dissolved in boiling water. The total weight of the mixture was controlled at the start and end of the boiling of the mixture. The evaporated amount of water was compensated by weight to ensure the planned concentration. The planned concentration ensures the stiffness of 25 kPa according to the Young modulus as predicted by HALL *et al.* (1997). To obtain scattering the powder prepared from a carbon tablet was used. We dispersed 1.05 g of the carbon powder in 1300 ml of the agar mixture. We continuously stirred the mixture with the carbon powder until it cooled down. Stirring prevented sedimentation of the carbon powder. At the start of gelation, the mixture was poured into the prepared container. Two pieces of metal pipe of 16 mm in diameter and about 90 mm in length were placed in the container. The thin-walled rubber vessel (diameter 7 mm, length 200 mm) was fixed to mimic the artery below these pipes. Both inclusions of approximately half the length of the rubber vessel were arranged along a single axis that is parallel to the axis of a vessel. Both ends of the rubber vessel were connected to flange fixtures in the walls of container, to allow the fluid to pass through. The bottom side of the container was covered with a 10 mm thick layer of foam below the rubber vessel. This foam layer acts as an absorber of ultrasound waves and allows one to

avoid multiple reflections of waves in the phantom. The schematic drawing of the phantom structure is presented in Fig. 1.
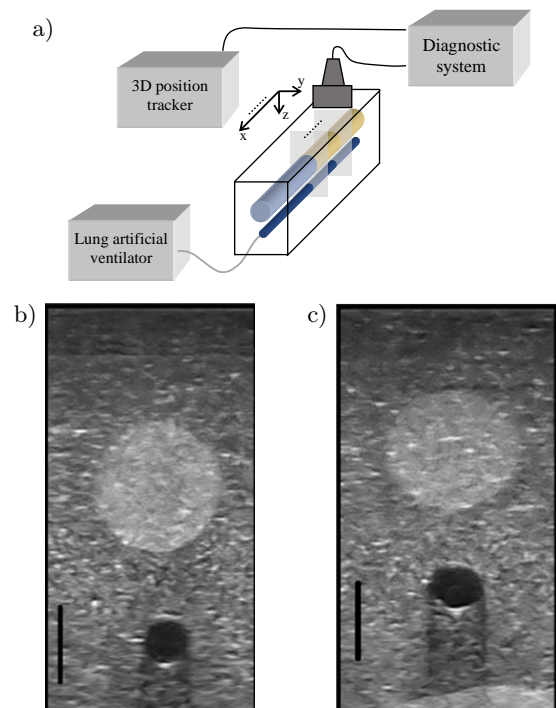

Fig. 1. Sketch of the experimental setup (a) and obtained B-scans (b, c): a) 3D freehand scanning for data recording (B-scan images, RF signals, and position sensor readings) for further volume rendering and 3D imaging of the inclusions; b) and c) B-scan images acquired with fixed probe from inclusions having similar acoustic (scattering) contrasting from background, but different mechanical (strain) properties. The black bar indicates 1 cm length.

The container was kept still to solidify at the refrigerator temperature for 1 hour. The container with a solid mixture of agar was further elaborated by implementing two inclusions. The pieces of metal pipe were filled with hot water to warm up and make the removal of the pipes from the agar mixture more slippery. Inclusions were made of agar concentrations 17.7 and 5 g/l (or predicted the Young modulus 75 kPa and 7 kPa, respectively) according to the same procedure as a background. Two mixtures of 100 ml each were added with 0.27 g of the carbon powder to make the waves scattering from inclusions stronger than the background material. At the beginning of gelation, the first mixture was poured into tunnel-like holes in the background. The phantom was kept still to solidify the agar mixture into the first inclusion. The implementation of the second inclusion was repeating the procedure of preparation of the first inclusion.

The thin-walled rubber vessel is intended to mimic the cardiovascular pulsations. The vessel was filled with distilled water and occluded in one end. The other end (the flange) was connected to the corru-

gated tubing of the artificial lung ventilation output. Pulsations in the elastic rubber vessel were induced by a ventilator operated in a pressure-controlled mode. The pressure pulsation amplitude in the rubber vessel was 32 mmHg, while the pulsing rate was 70 times per minute. Both (the soft and hard) inclusions were excited from the same pulsating vessel.

The access to the prepared tissue mimicking materials in the container was from an open top of the container. The linear array transducer was directed to send ultrasound waves from the top surface of the agar mixture downwards: crossing trough the one of inclusions and a rubber vessel (see Fig. 1a). B-scan images were obtained in a cross sections of inclusion and the rubber vessel (see Figs. 1b and 1c).

2.3. Experiment

Two experiments of RF scanning of the phantom were performed:

1) RF data acquisition keeping the probe fixed. The probe was fixed in a laboratory stand. The B-scan plane was directed orthogonally to the inclusions, observing to get cross-section images of them. The diameters of 16.3 ± 0.4 mm and 15.3 ± 1.2 mm for hard and soft inclusions correspondingly were measured from B-scan images when the probe was fixed,

2) freehand 3D RF scanning. The translation of the probe on a top surface of phantom was manual. The translation was guided by the frame to get a straight-line trajectory, which was approximately aligned in parallel to axis of X coordinates of the electromagnetic position tracker. The B-scan plane direction to the phantom was handled manually, ensuring center of the selected inclusion in the middle of the B-scan image. The probe translation was limited to 21 mm. Freehand translations along only the selected inclusion were used for processing, excluding imaging of other inclusions.

2.4. Collected data

The B-scans (174 frames for each recording) and raw corresponding RF signals were acquired and stored for offline processing. The electromagnetic tracking sensor measurements (x, y, z, α, β, γ) were also stored for each frame. The RF data matrixes were 3648 (samples) $\times$ 314 (scanning lines) $\times$ 174 (frames) in size, meanwhile the B-mode datasets were of $616 \times 820 \times 174$ size with an isotropic pixel size of 0.15 mm. In total 4 records were acquired and analyzed during the study (for both inclusions with a fixed probe and applying 3D freehand scanning).

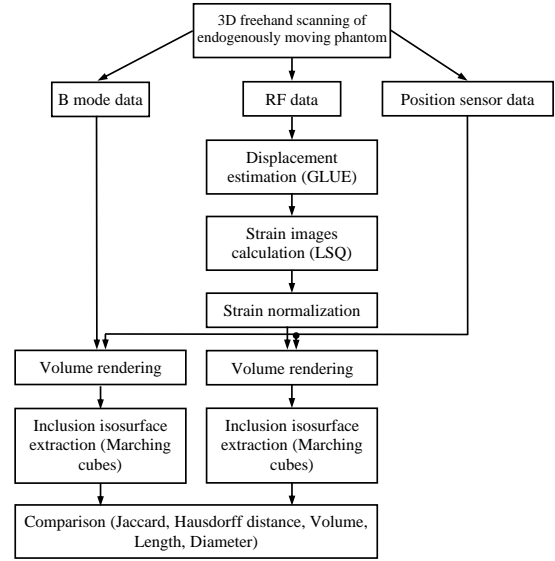The flow chart representing the concept of data processing in the study is presented in Fig. 2.

Fig. 2. Flowchart of the presented study: 3D freehand scanned data (B-mode images, RF signals, and position sensor readings) are used for volume rendering and 3D imaging of the inclusions having similar acoustic (scattering), but different mechanical (strain) properties, which are finally compared for the correspondence assessment.

2.5. Displacements estimation

Displacement images for consecutive frame pairs were obtained using the global time-delay estimation technique (GLUE) proposed by Hassan Rivaz group. The implementation and codes are provided by GLUE developers (HASHEMI, RIVAZ, 2017; RIVAZ et al., 2011). GLUE is a continuation of their work on time delay estimation, which at first were solved by the dynamic programming-based approach (RIVAZ et al., 2011). The GLUE algorithm refines the integer displacements estimates obtained by dynamic programming to a subsample accuracy. The subsample accuracy displacements are obtained in the axial and lateral directions. Overall, the displacement estimation algorithm has two stages: 1) estimation of integer displacements using dynamic programming; 2) GLUE: refinement of integer displacements to a subsample accuracy by minimizing the regularized cost function (presented in Eq. (1)).

The cost function for GLUE is formulated for the entire two-dimensional image (HASHEMI, RIVAZ, 2017):

$$C\left(\Delta a_{1,1}, ..., \Delta a_{m,n}, \Delta l_{1,1}, ..., \Delta l_{m,n}\right)$$

$$= \sum_{j=1}^{n} \sum_{i=1}^{m} \Big\{ \left[I_1(i,j) - I_2(i + a_{i,j} + \Delta a_{i,j}, j + l_{i,j} + \Delta l_{i,j})\right]^2$$

$$+ \alpha_1 \left(a_{i,j} + \Delta a_{i,j} - a_{i-1,j} - \Delta a_{i-1,j}\right)^2$$

$$+ \beta_1 \left(l_{i,j} + \Delta l_{i,j} - l_{i-1,j} - \Delta l_{i-1,j}\right)^2$$

$$+ \alpha_2 \left(a_{i,j} + \Delta a_{i,j} - a_{i,j-1} - \Delta a_{i,j-1}\right)^2$$

$$+ \beta_2 \left(l_{i,j} + \Delta l_{i,j} - l_{i,j-1} - \Delta l_{i,j-1}\right)^2 \Big\}, \tag{1}$$

where a is the initial integer axial displacements estimated by dynamic programming, l is the initial integer lateral displacements estimated by dynamic programming, α and β are the regularization terms, I_1 and I_2 are the consecutive RF data frames before and after the deformation, $i = 1, ..., m$, where m is the number of samples in RF scanning line, $j = 1, ..., n$, where n is the number of RF scanlines in the RF frame, Δ notes the subsample accuracy values for axial and lateral displacements. Displacements are usually very small, and subsample accuracy must be achieved.

For the presented study, the following values of the regularization coefficients were established: $\alpha_1 = \alpha_2 = 35.8$, and $\beta_1 = \beta_2 = 0.02$. The parameters of the dynamic programming algorithm were set as recommended by GLUE developers (Hashemi, Rivaz, 2017; Rivaz *et al.*, 2011). Only axial displacement images were used for further processing in our 3D approach, because it was found that the lateral displacement does not provide sufficient contrast for the analysis.

We recorded the data to evaluate and verify the frame-to-frame displacement waveform that we induced with pressure pulsations with a fixed array transducer in the first experiment. The spatial mean displacement was calculated from all points in the frame to evaluate the amplitude and shape of the excitation waveform. First, the average value for each displacement image was calculated, obtaining how the mean displacement varies over time. Next, the summed displacement signal was obtained by calculating the cumulative sum of the frame-to-frame displacement waveform. The summed displacement waveform was high-pass filtered (cut-off frequency 0.5 Hz) to remove the baseline drift.

2.6. Strain estimation

Strain images were obtained using the least squares regression (LSQ) technique as proposed by Hashemi and Rivaz (2017). The size of the differentiation kernel was 35 samples axially (0.67 mm), and 5 lines laterally (0.43 mm).

2.7. Strain normalization

Strain images were normalized (provided in Eq. (2)) to rescale them and to compensate for the strain differences, which arises due to the nature of endogenous compression that varies over time. The statistical normalization method was used:

$$S_N = \frac{S - \overline{S}}{\sigma_S}, \tag{2}$$

where S is the strain image before normalization, $\overline{S}$ is the mean value of the strain image, and σ_S is the standard deviation of the strain image.

2.8. Volume rendering

The rendering stage could be divided into three steps. Firstly, only in the case of 3D endogenous strain, some of the obtained images are acquired in a phase when the deformation is very low and insufficient to obtain a contrast between inclusion and the background. Such low signal-to-noise ratio (SNR) elastograms must be filtered out because otherwise the 3D volume will be affected by low SNR images. It is the fundamental limitation of the technique using harmonic natural strain, which sometimes becomes very close or even equal to zero. The empirical threshold was used for this purpose, all strain elastograms having mean strain lower than 0.03% were removed from the dataset. The threshold was established after visual revision of the sequences of strain images, when the majority of the selected frames, exceeding the threshold, provided a contrast for inclusions.

Secondly, the selected images (B-scans or strains elastograms) are arranged spatially according to the position sensor readings $(x_s, y_s, z_s, \alpha, \beta, \gamma)$. The 3D arrangement was done according to coordinates transformed by equation (Lee *et al.*, 2018):

$$\begin{bmatrix} x_t \\ y_t \\ z_t \end{bmatrix} = \begin{bmatrix} x_s \\ y_s \\ z_s \end{bmatrix} + \mathbf{C} \cdot \mathbf{R}(\alpha, \beta, \gamma) \cdot \begin{bmatrix} x_p \\ y_p \\ z_p \end{bmatrix}, \tag{3}$$

where (x_t, y_t, z_t) is the image point coordinates in the arranged 3D space, (x_s, y_s, z_s) is the position coordinates measured by the electromagnetic sensor (incorporated in the linear array), $\mathbf{C}$ is the calibration matrix for electromagnetic sensor and linear array setup (values provided by vendor), $\mathbf{R}(\alpha, \beta, \gamma)$ is the rotation matrix calculated (Eq. (4)) from the angles measured by an electromagnetic sensor, (x_p, y_p, z_p) is the point position in the image (in a coordinate system of linear array) before transform, p is the index of pixels in image data. B-scan images were of 616×820 size and strain elastograms were the same as the RF data frame in size. The rotation matrix is expressed as follows:

$$\mathbf{R}(\alpha, \beta, \gamma) = \begin{bmatrix} \cos(\alpha) \cdot \cos(\beta) & \cos(\alpha) \cdot \sin(\beta) \cdot \sin(\gamma) - \sin(\alpha) \cdot \cos(\gamma) & \cos(\alpha) \cdot \sin(\beta) \cdot \cos(\gamma) + \sin(\alpha) \cdot \sin(\gamma) \\ \sin(\alpha) \cdot \cos(\beta) & \sin(\alpha) \cdot \sin(\beta) \cdot \sin(\gamma) + \cos(\alpha) \cdot \cos(\gamma) & \sin(\alpha) \cdot \sin(\beta) \cdot \cos(\gamma) - \cos(\alpha) \cdot \sin(\gamma) \\ -\sin(\beta) & \cos(\beta) \cdot \sin(\gamma) & \cos(\beta) \cdot \cos(\gamma) \end{bmatrix}, \tag{4}$$

where α – azimuth, β – elevation, and γ – roll angles. So, the points with coordinates (x_p, y_p, z_p) from the B-scan plane are arranged at coordinates (x_t, y_t, z_t) in 3D space.

Thirdly, the arranged planes are mapped to a regular rectangular grid representing voxels. Standard MATLAB processing routine (griddata function) was used for the purpose of applying cubic interpolation for the irregularly spaced image data. The dimensions of the voxel were set to be $0.25 \times 0.25 \times 0.25$ mm³. The obtained 3D matrixes were filtered by the smoothing moving average filter ($9 \times 9 \times 9$ voxels).

2.9. Extraction of inclusion isosurface

Isosurfaces of the phantom inclusions were extracted for the visual assessment and quantitative comparison for both parametric 3D images (obtained from the B-mode and normalized strain). The marching cube algorithm (LORENSEN, CLINE, 1987) was used for extraction. The algorithm requires to set a threshold isovalue for the extraction of the volume enclosed by the isosurface. The threshold values were determined by using these criteria:

- for the B-mode the threshold was set above majority of randomly distributed parasitic reflections which occurs in the background region;
- threshold values were adjusted looking for the best correlation according to quantitative metrics between strain and reflection 3D isosurfaces;
- extracted isosurfaces were evaluated visually and the surface reconstruction was accepted only if there were no strong shape distortions, even if the quantitative results were better.

Threshold values for the B-mode: soft inclusion = 127, hard = 140; for normalized strain images: soft = 0.35 and hard = 0.63 were established. An example illustrating the selected threshold values and the resulting boundaries for these values (red contour) of the inclusions for both types (the B-mode and strain) of images is presented in Fig. 3.

2.10. Quantitative comparison

After volume rendering and isosurface extraction, two types of 3D images were obtained: first reconstructed from the B-mode data and based on acoustical property – reflections, and second reconstructed from the calculated strain elastograms and representing the mechanical property – stiffness. The 3D isosurfaces were superimposed. Five quantitative metrics were used for the assessment of the correspondence between 3D image of the reflections and the 3D image of strain:

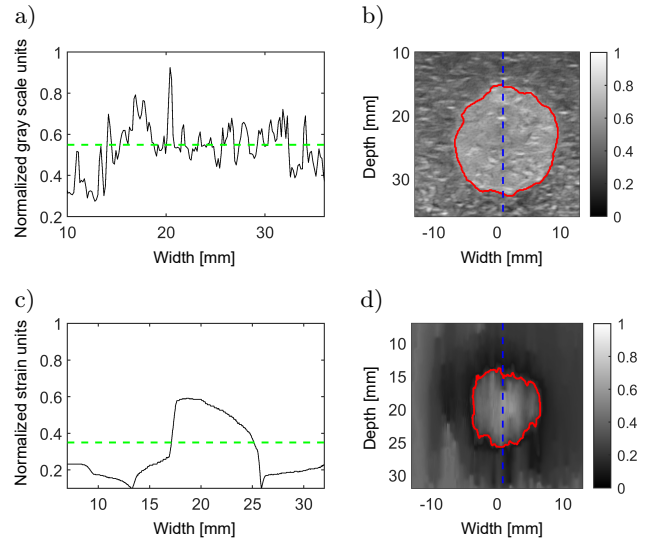- volumes calculated by summing voxels enclosed by isosurface;

Fig. 3. Threshold selection examples for B-mode image (a–b) and strain elastogram (c–d): a) shows single normalized gray scale intensity line crossing the middle of inclusion (marked by dashed blue line in part (b) superimposed on B-mode image) and threshold level is shown by green dashed line; b) shows B-mode image together with a contour (red color) extracted by using the threshold; c) and d) show exactly the same just for strain elastogram case.

- diameters of the inclusions estimated by the manual measurement (three repetitive measurements);
- lengths of the inclusions estimated by the manual measurement (three repetitive measurements);
- the Jaccard similarity coefficient, which is expressed as follows:

$$\text{Jaccard} = \frac{|A \cap B|}{|A \cup B|}, \qquad (5)$$

where A and B are the volumes obtained from images having different properties (the B-mode and endogenous normalized strain);

- the Hausdorff distance – which measures the largest distance between paired points of the extracted isosurfaces. It is found by using the following Eqs. (6) and (7). Firstly, the one-sided Hausdorff distance is found for both isosurfaces:

$$h(\mathbf{A}, \mathbf{B}) = \max_{\mathbf{a} \in \mathbf{A}} \min_{\mathbf{b} \in \mathbf{B}} \|\mathbf{a} - \mathbf{b}\|, \qquad (6)$$

here $\mathbf{A}$ and $\mathbf{B}$ are the points cloud coordinates (x, y, z) of the extracted isosurfaces obtained from images of different properties (the B-mode and endogenous normalized strain), $\mathbf{a} = \{x_1, y_1, z_1, ..., x_n, y_n, z_n\}$, and $\mathbf{b} = \{x_1, y_1, z_1, ..., x_m, y_m, z_m\}$, m, n are the numbers of points in data clouds. Next, the bidirectional Hausdorff distance H is calculated by Eq. (7):

$$H(\mathbf{A}, \mathbf{B}) = \max(h(\mathbf{A}, \mathbf{B}), h(\mathbf{BA})). \qquad (7)$$

3. Results

At first, the excitation waveform of endogenous phantom displacements was evaluated from the first experiment when the array transducer was fixed during RF recording. Figure 4 presents the summed mean displacement versus time.
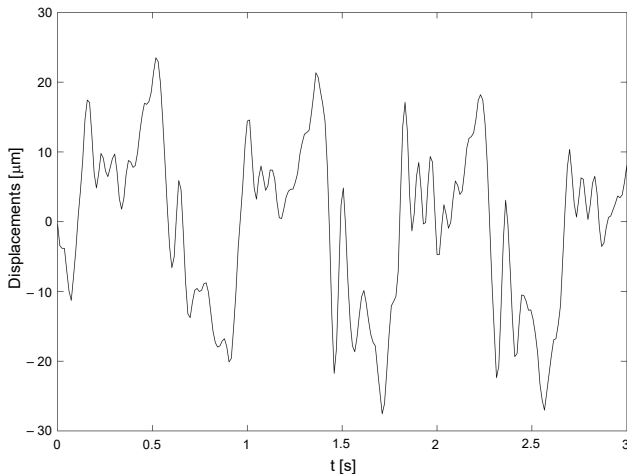

Fig. 4. Comparison of averaged in-space summed phantom displacements (3.5 periods, first 3 seconds). The displacements were estimated from the experiment with fixed array transducer.

The periodicity of the waveform is noticeable. The amplitude of frame-averaged displacements reaches 20 µm. The period of the waveform of the induced displacements matches the rate of the ventilation apparatus (70 times per minute).

Figure 5 presents the examples of normalized 2D strain images (S_N) obtained in the second experiment (freehand 3D scanning) at the time of maximum normalized mean strain.

It could be seen that both inclusions (hard – 75 kPa and soft – 7 kPa) could be clearly identified. The contrast between inclusion and background was a bit larger for a soft inclusion. It is observable that the inclusions are slightly deformed and non-circular, but the contrasts are sufficient for imaging purposes. However, after a visual analysis of all (of time instances) strain images (S_N) in the 3D dataset, it was found that only about 25% of the 2D strain images provided a sufficient contrast (mean strain of the frame > 0.03%) for 3D rendering. Therefore, the mean strain parameter was proposed as a criterion to filter low contrast strain images and remove about 75% of them from the 3D dataset, before 3D rendering.

The cross-sectional images of both inclusions of the phantom rendered volumes are presented in Fig. 6.

Figures 7 and 8 present the extracted isosurfaces of cylindrical inclusions.

Figure 7 shows the inclusions extracted from the 3D datasets of the imitated endogenous strain. It could be observed that the inclusions do not follow the exact
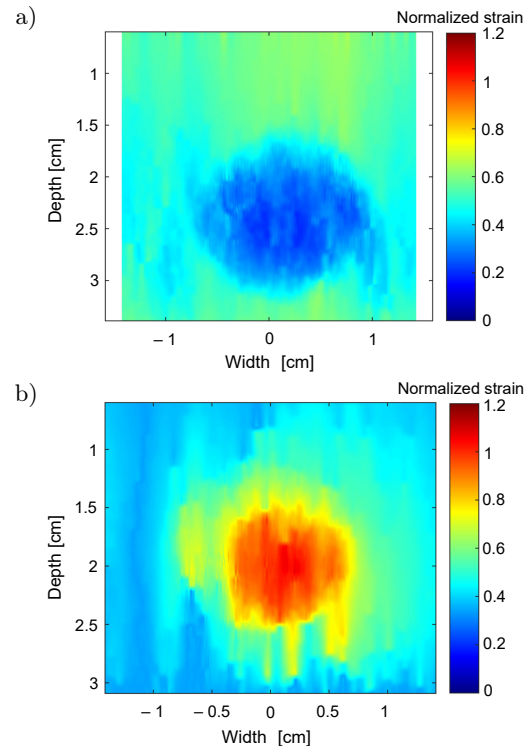

Fig. 5. The 2D examples of normalized strain elastograms of the phantom containing (a) hard inclusion and (b) soft inclusion.
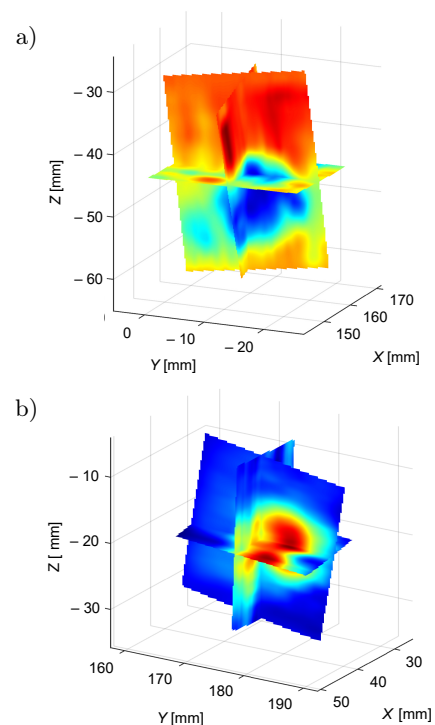

Fig. 6. Cross-sectional images of 3D strain elastograms for the phantom containing (a) hard inclusion and (b) soft inclusion.

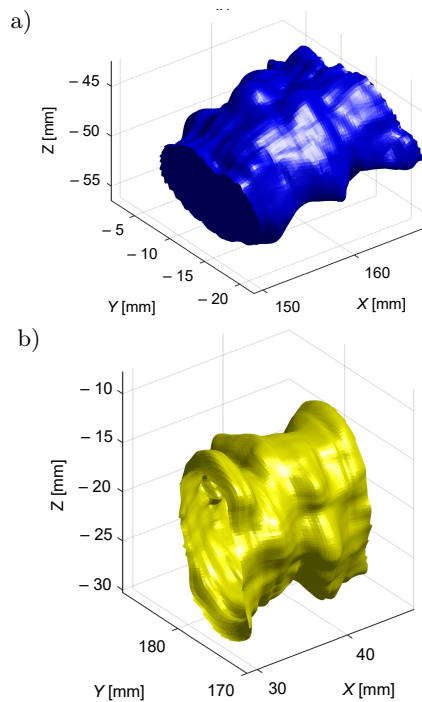shape of the cylinder, but at the same time they are relatively smooth.

a)

b)

Fig. 7. Results of 3D isosurface imaging for (a) hard and (b) soft inclusions (images obtained from strain elastography data).
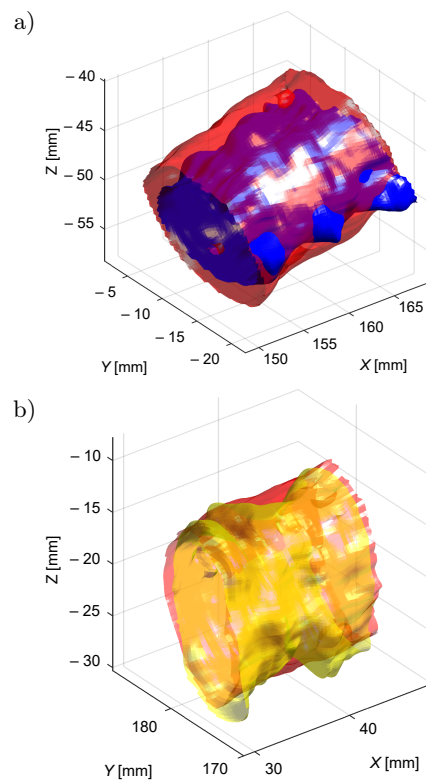
a)

b)

Fig. 8. Comparison of isosurfaces obtained from volumes reconstructed from B-mode (red) and normalized strain images for (a) hard (blue) and (b) soft (yellow) inclusions.

A comparison between the isosurfaces extracted from the B-mode image dataset and normalized strain images (Fig. 8) showed that the volume of strain-based 3D image was underestimated. For both inclusions, the volumes were smaller in the case of rendering from strain images. The hard inclusion in Fig. 8a was less correlated with the reference obtained from the B-mode image dataset, in comparison to the soft one (Fig. 8b).

The quantitative results of comparison of inclusions obtained by 3D imaging of reflections and strain are presented in Table 1.

The volumes obtained from strain elastograms were smaller in comparison to those obtained from the B-mode (remarkably about 30% for the hard inclusion and a bit less for the soft one ~15%). The correspondence between the volume of inclusion based on B-mode images and the volume based on strain elastography was good (the Jaccard coefficient within the range 0.64–0.74).

The comparison of diameters and lengths showed that the diameter value is less correlated with the measured from the isosurface obtained from B-mode images than the length for both inclusions. The Jaccard similarity coefficient and the Hausdorff distance shows that the isosurface of the soft inclusion was in better correlation to the isosurface obtained from the B-mode dataset.

4. Discussion

The obtained results confirm the endogenous motion-based elastography as a feasible technique. The 3D freehand visualization of the inclusions by the strain was successful. Thresholding of strain dataset proved as sufficient with elastograms of at least 0.03% of the mean strain. To the best of our knowledge, there

Table 1. Quantitative comparison of obtained dimensions and volumes.

		Volume rendered from 3D data [mm³]	Diameter from 3D data [mm]	Length [mm]	Diameter from static data [mm]	Jaccard similarity coefficient	Hausdorff distance [mm]
Hard inclusion [75 kPa]	Reflections	2832.2	13.92 ± 1.65	14.10 ± 0.47	16.30 ± 0.40	0.64	4.85
	Strain	1970.0	13.02 ± 2.66	15.53 ± 0.21	15.98 ± 1.27		
Soft inclusion [7 kPa]	Reflections	2744.1	15.30 ± 1.77	16.08 ± 0.29	15.30 ± 1.20	0.74	3.77
	Strain	2361.5	14.46 ± 2.94	15.26 ± 0.48	12.34 ± 1.20		

is no published data about the results of endogenous strain 3D imaging, so it is hard to discuss in a direct comparison and to make a comparison with an existing technique. The range of strain for 3D imaging was evaluated by HAVRE *et al.* (2017), but for the case of real-time elastography. In their study, sufficient strains levels were found in range of approximately 0.1% to 2% for the by hand deformations of phantom. Our in vitro pilot achievement is obtained not by external sources of deformations, but by internal sources and with an even smaller strain of only >0.03%. Our findings show that soft inclusion was in better correspondence with the reference obtained from B-scans in comparison to hard inclusion. However, the discrepancy of quantitative estimates shows the limitations of our method studied. In general, the freehand 3D imaging with ultrasound is found to result in discrepancies as reviewed by MOZAFFARI and LEE (2017). They reviewed that with the electromagnetic positioning system the volume estimation accuracy errors from 1.1% to 5.44% are possible. These accuracies are reviewed for the cases with B-scan images obtained in vitro. In our case, only discrepancies of estimates between B-scan images and strain images are possible, as we used in-lab-made phantoms of non-verified dimensions. Both inclusions were found to be smaller when the isosurfaces and volumes extracted from the reflection image data and the strain image data were compared. The volumes of elasticity obtained were smaller by up to 30% compared to volumes reconstructed with B-scan. This total discrepancy includes the level of about 5% of volume estimation accuracy that is a common feature for 3D ultrasonic imaging with an electromagnetic positioning system. So about 25% discrepancy we attribute to the strain image reconstruction. Strain volumes were estimated to be smaller than volumes reconstructed from B-scans, and this is contrary to (LEE *et al.*, 2018). The 3D freehand ultrasound elastography study, where the measured volumes were highly correlated with reference values in a commercial phantom. The absolute values of the volumes and dimensions (provided in Table 1) used for comparison were estimated from the measurements based on the scanning data. Although ultrasound velocity in the phantom base material and inclusions might be different and not exactly known, the scanner setting for velocity is standard – 1540 m/s, as always in clinical practice. Therefore, the estimates calculated assuming the uniform speed 1540 m/s, have deviation from the real values. From B-scan images, obtained with a fixed probe, diameters of inclusions, we found a little distorted from a round shape: the hard inclusion dimensions in X and Y directions were 16.3 ± 0.4 mm, that is 2.5% distortion from the round shape, and for soft inclusion 15.3 ± 1.2 mm the 7.8% distortion from the round shape. The variations of a sound speed in agar mixtures of the similar magnitude were found

(BURLEW *et al.*, 1980; MADSEN *et al.*, 1998). So, we attribute the diameter discrepancies to uncertainty of the sound speed in agar mixtures. Distortions from the round shape of inclusion diameters in strain images are much more significant, that we originate from strain imaging peculiarities which have not been discovered yet.

The preparation of inclusions intended a threefold difference in stiffness of agar mixtures. The soft inclusion was 7 kPa versus 25 kPa stiffness of the background material, or 3.6 times difference. This possibly resulted the contrast between inclusion and background was a bit larger for soft inclusion in 2D elastograms. The hard inclusion was 75 kPa versus 25 kPa, so the stiffness ratio was 3 times.

The endogenous motion is relatively weak in comparison to compressions induced by the ultrasound probe, but has potential for the assessment of deeper layers of tissue. It should be noted that the amplitude of the imitated displacements reached only 20 μm (Fig. 4), meanwhile we have found it to be close to 100 μm in the specific segment of the liver, close to the beating heart, in a previous study (SAKALAUSKAS *et al.*, 2016). The better contrast of the strain elastogram could be expected for larger displacement amplitude. Researchers (LEE *et al.*, 2018) have indicated that the 3D freehand elastography using probe compressions suffers from respiratory and cardiac motion artefacts, which is not the case for the presented technique where the cardiac activity will serve as an excitation source.

5. Limitations of the study

We have identified few limitations of the study. Firstly, the inclusions in the laboratory-prepared phantom had a relatively high stiffness difference in comparison to the background (75 kPa and 7 kPa in contrast to 25 kPa). The approach of phantom preparation requires a relatively stiff background material that can hold its form. The very soft (less 25 kPa) background material does not allow the implementation of inclusions as hanging structures above the rubber vessel. We have plans to manufacture a phantom of a different structure, having the soft background material and inclusions closer to the background in stiffness. In future studies, the new structure phantom would enable evaluating the potential stiffness contrasting possibilities of the technique. The presented study was just a first step proof of a concept, confirming the method as promising.

Secondly, the trajectory of a freehand probe motion in our case was approximately linear. Only axial displacements were evaluated in our study, the lateral and respectively strain in that direction do not provide sufficient contrast for 3D rendering. Using other, more complicated trajectories possibly will introduce differ-

ent 3D reconstruction errors, although the 3D rendering method (Eqs. (3) and (4)) allows free trajectories of any shape. We hypothesize, that the lateral sampling (more scanning lines) could be employed in the future studies. As well the lateral displacements, that are possible to detected with the GLUE algorithm, could provide an extra contrast in the elastogram from lateral strain.

Thirdly, the low strain elastograms were filtered by using a relatively simple technique – the mean strain value threshold, and it was noticed that some elastograms selected after filtering do not provide high contrast of the inclusion. These elastograms affected the final precision of the isosurface of the inclusion dimensions and the volume estimates. We have shown the technique to be feasible, however, we have to admit that the endogenous motion of the cylindrical shape of source is still too simple an approximation of the in vivo case. The properties of rubber vessels were not controlled in the experiments, while the stiffness of blood vessels has its own physiological behavior in vivo. Time waveforms of endogenous displacements and their frequency spectrum features which have been found related to a waveform pattern of an excitation pressure. The surrogate waveform induced in the phantom needs adjustments to the waveform features of in vivo displacements. Thus, living tissue requires further investigation, which can allow for a more reliable selection of frames for 3D rendering. It was found that the low mean strain of the frame is not always followed by a low contrast elastogram and vice versa. Such findings are still difficult to explain and will be investigated more widely in future studies. Repeatability of the method was not evaluated. However, we still recall that this pilot study was conducted just to evaluate the feasibility of performing 3D imaging of endogenous strain.

6. Conclusion

The results obtained confirm the endogenous motion-based 3D elastography as a feasible technique. The freehand 3D visualization of the inclusions by the strain was successful. However, quantitative measurements showed that the accuracy of the method in volumetric measurements is limited.

Declarations

The authors declare that they have no conflicts of interest. This article does not contain any studies with human or animal subjects performed by any of the authors.

Acknowledgments (funding)

References

1. ABEYSEKERA J., ROHLING R., SALCUDEAN S. (2015), Vibro-elastography: Absolute elasticity from motorized 3D ultrasound measurements of harmonic motion vectors, [in:] *2015 IEEE International Ultrasonics Symposium (IUS)*, pp. 1–4, doi: 10.1109/ULTSYM.2015.0201.

2. BAE U., DIGHE M., SHAMDASANI V., MINOSHIMA S., DUBINSKY T., KIM Y. (2006), 6F-6 thyroid elastography using carotid artery pulsation: A feasibility study, [in:] *2006 IEEE Ultrasonics Symposium*, pp. 614–617, doi: 10.1109/ULTSYM.2006.160.

3. BARR R.G. *et al.* (2017), WFUMB guidelines and recommendations on the clinical use of ultrasound elastography: Part 5. Prostate, *Ultrasound in Medicine and Biology*, **43**(1): 27–48, doi: 10.1016/j.ultrasmedbio.2016.06.020.

4. BERCOFF J., SINKUS R., TANTER M., FINK M. (2004), 3D ultrasound-based dynamic and transient elastography: First in vitro results, [in:] *IEEE International Ultrasonics Symposium*, **1**: 28–31, doi: 10.1109/ULTSYM.2004.1417660.

5. BURLEW M.M., MADSEN E.L., ZAGZEBSKI J.A., BANJAVIC R.A., SUM S.W. (1980), A new ultrasound tissue-equivalent material, *Radiology*, **134**(2): 517–520, doi: 10.1148/radiology.134.2.7352242.

6. CHEN Z., CHEN Y., HUANG Q. (2016), Development of a wireless and near real-time 3D ultrasound strain imaging system, *IEEE Transactions on Biomedical Circuits and Systems*, **10**(2): 394–403, doi: 10.1109/TBCAS.2015.2420117.

7. COSGROVE D. *et al.* (2017), WFUMB guidelines and recommendations on the clinical use of ultrasound elastography: Part 4. Thyroid, *Ultrasound in Medicine & Biology*, **43**(1): 4–26, doi: 10.1016/j.ultrasmedbio.2016.06.022.

8. DICKINSON R.J., HILL C.R. (1982), Measurement of soft tissue motion using correlation between A-scans, *Ultrasound in Medicine & Biology*, **8**(3): 263–271, doi: 10.1016/0301-5629(82)90032-1.

9. DIETRICH C.F. *et al.* (2017), Strain elastography – How to do it?, *Ultrasound International Open*, **3**(4): E137–E149, doi: 10.1055/s-0043-119412.

10. GELMAN S. *et al.* (2020), Endogenous motion of liver correlates to the severity of portal hypertension, *World Journal of Gastroenterology*, **26**(38): 5836–5848, doi: 10.3748/wjg.v26.i38.5836.

11. GILJA O.H., HAUSKEN T., OLAFSSON S., MATRE K., ØDEGAARD S. (1998), In vitro evaluation of three-dimensional ultrasonography based on magnetic scan head tracking, *Ultrasound in Medicine & Biology*, **24**(8): 1161–1167, doi: 10.1016/S0301-5629(98)00098-2.

12. HALL T.J., BILGEN M., INSANA M.F., KROUSKOP T.A. (1997), Phantom materials for elastography, *IEEE Transactions on Ultrasonics, Ferroelectrics, and Frequency Control,* **44**(6): 1355–1365, doi: 10.1109/58.656639.

13. Hashemi H.S., Rivaz H. (2017), Global time-delay estimation in ultrasound elastography, *IEEE Transactions on Ultrasonics, Ferroelectrics, and Frequency Control*, **64**(10): 1625–1636, doi: 10.1109/TUFFC.2017.2717933.

14. Havre R.F. *et al.* (2008), Freehand real-time elastography: Impact of scanning parameters on image quality and in vitro intra- and interobserver validations, *Ultrasound in Medicine & Biology*, **34**(10): 1638–1650, doi: 10.1016/j.ultrasmedbio.2008.03.009.

15. Hendriks G.A.G.M., Holländer B., Menssen J., Milkowski A., Hansen H.H.G., de Korte C.L. (2016), Automated 3D ultrasound elastography of the breast: A phantom validation study, *Physics in Medicine & Biology*, **61**(7): 2665–2679, doi: 10.1088/0031-9155/61/7/2665.

16. Housden R.J., Gee A.H., Treece G.M., Prager R.W. (2010), 3-D ultrasonic strain imaging using freehand scanning and a mechanically-swept probe – correspondence, *IEEE Transactions on Ultrasonics, Ferroelectrics, and Frequency Control*, **57**(2): 501–506, doi: 10.1109/TUFFC.2010.1431.

17. Huang Q., Xie B., Ye P., Chen Z. (2015), Correspondence – 3-D ultrasonic strain imaging based on a linear scanning system, *IEEE Transactions on Ultrasonics, Ferroelectrics, and Frequency Control*, **62**(2): 392–400, doi: 10.1109/TUFFC.2014.006665.

18. Kolen A.F., Miller N.R., Ahmed E.E., Bamber J.C. (2004), Characterization of cardiovascular liver motion for the eventual application of elasticity imaging to the liver in vivo, *Physics in Medicine & Biology*, **49**(18): 4187–4206, doi: 10.1088/0031-9155/49/18/001.

19. Lee F.-F., He Q., Luo J. (2018), Electromagnetic tracking-based freehand 3D quasi-static elastography with 1D linear array: A phantom study, *Physics in Medicine & Biology*, **63**(24): 245006, doi: 10.1088/1361-6560/aaefae.

20. Lindop J.E., Treece G.M., Gee A.H., Prager R.W. (2006), 3D elastography using freehand ultrasound, *Ultrasound in Medicine & Biology*, **32**(4): 529–545, doi: 10.1016/j.ultrasmedbio.2005.11.018.

21. Lorensen W.E., Cline H.E. (1987), Marching cubes: A high resolution 3D surface construction algorithm, [in:] *Proceedings of the 14th Annual Conference on Computer Graphics and Interactive Techniques*, **21**(4): 163–169, doi: 10.1145/37401.37422.

22. Luo S., Kim E.-H., Dighe M., Kim Y. (2009), Screening of thyroid nodules by ultrasound elastography using diastolic strain variation, [in:] *2009 Annual International Conference of the IEEE Engineering in Medicine and Biology Society*, pp. 4420–4423, doi: 10.1109/IEMBS.2009.5332744.

23. Madsen E.L., Frank G.R., Dong F. (1998), Liquid or solid ultrasonically tissue mimicking materials with very low scatter, *Ultrasound in Medicine & Biology*, **24**(4): 535–542, doi: 10.1016/s0301-5629(98)00013-1.

24. Mai J.J., Insana M.F. (2002), Strain imaging of internal deformation, *Ultrasound in Medicine & Biology*, **28**(11–12): 1475–1484, doi: 10.1016/S0301-5629(02)00645-2.

25. Mozaffari M.H., Lee W.-S. (2017), Freehand 3-D ultrasound imaging: A systematic review, *Ultrasound in Medicine & Biology*, **43**(10): 2099–2124, doi: 10.1016/j.ultrasmedbio.2017.06.009.

26. Richards M.S., Barbone P.E., Oberai A.A. (2009), Quantitative three-dimensional elasticity imaging from quasi-static deformation: A phantom study, *Physics in Medicine & Biology*, **54**(3): 757–779, doi: 10.1088/0031-9155/54/3/019.

27. Rivaz H., Boctor E.M., Choti M.A., Hager G.D. (2011), Real-time regularized ultrasound elastography, *IEEE Transactions on Medical Imaging*, **30**(4): 928–945, doi: 10.1109/TMI.2010.2091966.

28. Sakalauskas A., Jurkonis R., Gelman S., Lukoševičius A., Kupčinskas L. (2016), Initial results of liver tissue characterization using endogenous motion tracking method, [in:] *Conference Proceedings Biomedical Engineering*, pp. 132–137, http://biomed.ktu.lt/index.php/BME/article/viewFile/3392/150.

29. Sakalauskas A., Jurkonis R., Gelman S., Lukoševičius A., Kupčinskas L. (2018), Development of radiofrequency ultrasound based method for elasticity characterization using low frequency endogenous motion: Phantom study, [in:] *IFMBE Proceedings*, Eskola H., Väisänen O., Viik J., Hyttinen J. [Eds.], Springer Singapore, pp. 474–477, doi: 10.1007/978-981-10-5122-7_119.

30. Sakalauskas A., Jurkonis R., Gelman S., Lukoševičius A., Kupčinskas L. (2019), Investigation of radiofrequency ultrasound-based fibrotic tissue strain imaging method employing endogenous motion: Endogenous motion-based strain elastography, *Journal of Ultrasound in Medicine*, **38**(9): 2315–2327, doi: 10.1002/jum.14925.

31. Tristam M., Barbosa D.C., Cosgrove D.O., Nassiri D.K., Bamber J.C., Hill C.R. (1986), Ultrasonic study of in vivo kinetic characteristics of human tissues, *Ultrasound in Medicine & Biology*, **12**(12): 927–937, doi: 10.1016/0301-5629(86)90061-x.

32. Wang Y., Spangler C.H., Tai B.L., Shih A.J. (2013), Positional accuracy and transmitter orientation of the 3D electromagnetic tracking system, *Measurement Science and Technology*, **24**(10): 105105–105113, doi: 10.1088/0957-0233/24/10/105105.

33. Wells P.N.T., Liang H.-D. (2011), Medical ultrasound: Imaging of soft tissue strain and elasticity, *Journal of the Royal Society Interface*, **8**(64): 1521–1549, doi: 10.1098/rsif.2011.0054.

34. Wilson L.S., Robinson D.E. (1982), Ultrasonic measurement of small displacements and deformations of tissue, *Ultrasonic Imaging*, **4**(1): 71–82, doi: 10.1016/0161-7346(82)90006-2.

35. Zambacevičienė M., Jurkonis R., Gelman S., Sakalauskas A. (2019), RF ultrasound based estimation of pulsatile flow induced microdisplacements in phantom, [in:] *World Congress on Medical Physics and Biomedical Engineering 2018*, Lhotska L., Sukupova L., Lacković I., Ibbott G.S. [Eds.], Springer Singapore, pp. 601–605, doi: 10.1007/978-981-10-9035-6_112.